



Computational Analysis of Isolated and Embedded Ducted Rotors in Edgewise Flight

Matthew P. Misiorowski*, Farhan Gandhi†, and Assad A. Oberai‡
Rensselaer Polytechnic Institute, Troy, New York, 12180

This study examines the performance of an isolated and embedded-in-body ducted rotor in edgewise flight conditions. The flow over a three-dimensional model of ducted rotor configurations was simulated using the Spalart-Allmaras RANS model implemented in a stabilized finite element method. A sliding mesh was used to conveniently account for the large-scale motion associated with rotor revolutions. The simulation results were analyzed to understand the flow physics and quantify the contributions of the rotor and various sections of the duct interior surfaces on the total aerodynamic forces (thrust, drag, and side force) and moments (pitching and rolling). Performance comparisons were made between the isolated and embedded configurations. In cruise, the isolated duct configuration was shown to have a larger region of separated flow off the front inlet. The separation region in both configurations induces upwash through the front of the disk resulting in higher thrust production in that region but this effect is reduced in the embedded configuration. The front inlet and the rear diffuser are the major contributors to duct H-force but the embedded duct configuration produces lower total H-force. Both the duct and rotor contribute to a nose-up pitching moment, both of which are weaker for the embedded configuration. The rotor is the primary source of vertical vibratory forces as well as vibratory pitching moment. The small tip clearance of the rotor causes a local interaction between the blade tip and duct that is the dominant contributor to H-force vibratory forces on the ducted rotor. The embedded configuration was shown to significantly reduce the magnitude of the H-force and pitching moment vibrations, while vertical vibrations were largely the same for both configurations.

I. Nomenclature

α	=	Effective angle of attack of the duct cross-section
CFL Number	=	Courant–Friedrichs–Lewy Condition necessary for convergence
d	=	Length of diffuser section
D_E	=	Effective Drag
δ	=	Rotor blade tip clearance to duct wall
γ	=	Angle made by diffuser from vertical (Z) direction
L	=	Lift
R	=	Rotor radius
r	=	Radius of duct inlet curvature
S_x	=	Blade root shear in the chordwise direction
S_z	=	Blade root shear in the vertical direction
θ	=	Nose down attitude of ducted rotor
$y+$	=	Non-dimensional distance used to describe mesh fineness

II. Introduction

DUCTED rotor designs are attractive to modern rotorcraft designers. Novel designs like the Boeing Phantom Swift, the Urban Aeronautics X-Hawk, and the Aurora Flight Sciences Lightning Strike employ ducted fans to provide

*PhD Candidate, AIAA Student Member

†Professor, AIAA Associate Fellow

‡Professor

some vertical takeoff and landing (VTOL) capability and in some cases as ducted propellers (Refs. 1–3). Ducted fans provide an element of safety over open rotors which makes them desirable for manned vehicles and missions operating near people or buildings.

Ducts have been shown to increase the power loading for a rotor by expanding the rotor wake through a diffuser section, reducing the induced power (Ref. 4). Although the expansion of the rotor wake reduces the thrust produced by the rotor, air is drawn by the rotor over the duct inlet, causing a suction similar to the lift generated on the leading edge of an airfoil and provides additional thrust. In a well-designed duct, this additional lift will overcompensate for the reduction in rotor thrust, resulting in a ducted rotor that operates at a higher power loading than the same rotor in isolation.

While ducted rotors have proven aerodynamic advantages in hover, they experience large drag and pitching moments in forward flight. When the edgewise flight velocity dominates the inflow velocity, the front of the duct has a large angle of attack and behaves like an airfoil in deep stall, producing large amounts of lift but with flow separation close to the leading edge of the inlet (Ref. 5). Prior experimental and computational research has been conducted analyzing the performance of ducted fans in axial and edgewise flight as well as specific duct designs attempting to mitigate the deep stall behavior of the upstream section of the duct.

Pereira and Chopra (Refs. 6, 7) parameterized the duct geometry by inlet curvature, diffuser length and diffuser angle and measured the forces and moments acting on the ducted rotor in axial and edgewise flight. This experiment established trends in ducted rotor performance based on these geometric parameters. The results showed how increasing the radius of curvature of the inlet could delay the separation point on the upstream duct inlet.

Hook, Myers and McLaughlin (Refs. 8, 9) performed experiments on a tandem ducted fan design with two ducted fans arranged longitudinally in the body of an air vehicle. Forces and moments acting on the aircraft were measured and the inlet shape on the front duct was changed attempting to improve vehicle performance. Using flow visualization techniques, this experiment confirmed that altering the inlet design could reduce the separation region on the upstream duct inlet but it did not significantly affect the aircraft lift or drag. Martin and Tung performed wind tunnel experiments on an isolated ducted fan in axial and edgewise flight. This experiment recorded the forces and moments acting on the ducted fan while the duct inlet curvature was varied (Ref. 10). The experiment also examined the effect of rotor tip clearance with the duct wall. When the rotor RPM was varied in this study, the angle of attack at which stall occurs on the upstream duct inlet changed significantly, proving that a high induced velocity is required to help keep flow attached to the duct inlet in edgewise flight. Martin and Boxwell further investigated the effect tip clearance has on ducted rotor performance by testing notches in the interior of the duct in the rotor plane. (Ref. 11). Ultimately, the notched duct designs did not significantly change the ducted rotor performance.

Akturk and Camci (Refs. 12–14) used a combination of experimental and computational methods to analyze ducted fans. Particle image velocimetry (PIV) and wind tunnel experiments were conducted on ducted fans in hover and edgewise flight. These experiments showed that a significant portion of the inflow distribution was affected by the size of the separation bubble on the upstream duct inlet. Further computational analysis was conducted by this group to analyze the effect of rotor tip shapes and a double ducted fan design using computational fluid dynamics (CFD). It was found that decreasing tip clearance improved the performance of the ducted fan and the double ducted fan design is a viable duct inlet separation control device.

The US Army Research Laboratory has conducted computational analysis of ducted fans. Singh and Dinavahi (Ref. 15) coupled CFD analysis with an optimization scheme to design the ideal duct shape. Jimenez and Singh (Ref. 16) used CFD analysis to compare the performance of two different rotor and duct geometry pairs. The first study developed a polynomial surrogate model that was able to predict rotor system performance with 3% of the CFD solution. The second study shows that an untwisted rotor performed more efficiently as a ducted rotor than a rotor with ideal twist. This effect comes from the added downwash on the rotor due to the presence of the duct. Both of these computational studies only looked at axial flow of a ducted rotor in hover.

Misiorowski, Gandhi, and Oberai (Refs. 17) used computational analysis to examine isolated ducted rotors in hover and edgewise flight. These CFD simulations identified dominant flow physics that drove the integrated performance metrics such as forces and moments. Additionally, the results examined interactions between the rotor and duct aerodynamics and their contribution to vibratory forces at the blade passage frequency.

While prior research has investigated the performance and flow physics of an isolated ducted rotor, the effect on the performance from embedding the duct in a fuselage or aerodynamic fairing is not fully understood. The isolated and embedded ducts have distinct inlet geometry which will affect the flow physics of the system and warrants an investigation into the trade-offs between the two designs. The present study uses CFD tools to solve the unsteady Reynolds Averaged Navier-Stokes (URANS) equations to provide a quantitative comparison of the performance of the

two duct configurations and visualize complex flow features at various regions in the ducted rotor system. The study includes a performance comparison of the two configurations in hover and at 10 m/s forward flight speed. Integrated performance metrics such as forces and moments on the ducted rotors and their decomposition will be presented along with a detailed analysis of the flow physics and interactions between the rotor and duct. Lastly, this study examines the dominant vibratory loading associated with blade passage frequency and the duct contribution to these loads.

III. Method

A. Coordinate System

This study uses a South, East, Up right-handed coordinate system. The $+X$ is the direction of aircraft drag (or H-force), $+Y$ is out the “right wing” or $\Psi = 90^\circ$ and $+Z$ is in the upward vertical direction.

B. Ducted Rotor Models

This paper presents the results of a representative ducted rotor configuration. The duct geometry was based on the experiments of Pereira which parameterizes the duct geometry by the inlet radius of curvature, length of the diffuser section, and angle of the diffuser section (Ref. 6, 7). Figure 1 and Figure 2 provide to-scale drawings of the ducted rotor configurations describing the duct design parameters, which are given as percentages of the rotor radius (R).

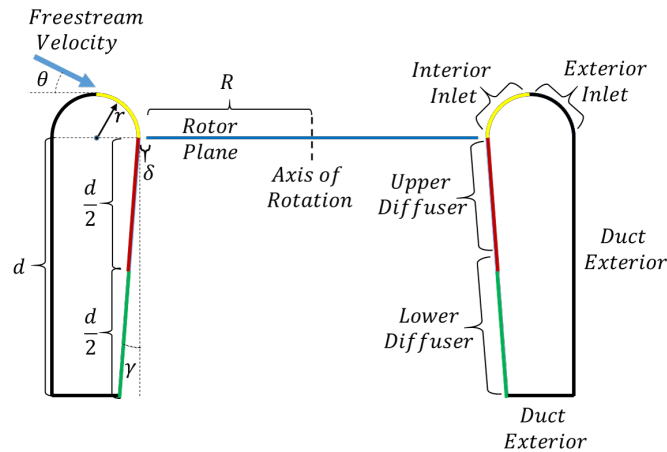


Fig. 1 Schematic of isolated ducted rotor system with parameters describing duct geometry

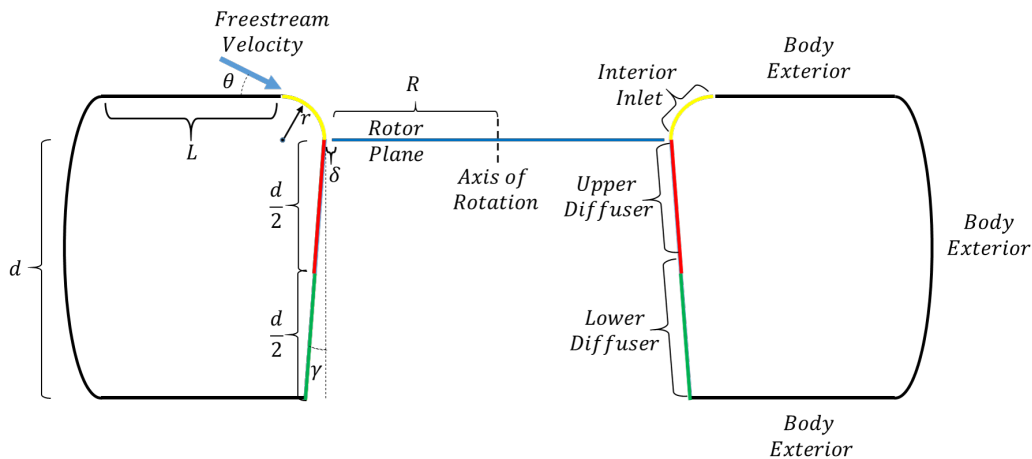


Fig. 2 Schematic of embedded ducted rotor system with parameters describing duct geometry

The parameter r (26% R) represents the radius of the semicircular inlet section, d (144% R) represents the length of the entire diffuser section, and γ (0°) is the diffuser angle. The parameter δ (1% R) is exaggerated in the figure to become visible and represents the clearance between the rotor tip and duct wall, and R (15.24 cm) is the rotor radius. The angle θ (0°) is the relative nose down attitude of the ducted rotor relative to the freestream. The duct was discretized along the axial direction into three surfaces shown in Figure 1 and Figure 2: the interior inlet (yellow), the upper diffuser (red) and the lower diffuser (green). This discretization of the duct surfaces facilitates more accurately determining the location of acting forces and moments. In addition to discretizing the duct in the axial direction, each of the surfaces is divided azimuthally in 5° increments which provides resolution for determining where around the duct the greatest forces act. While the duct geometry for both configurations is based on Refs. 6, 7, the duct from Figure 1 was the focus of a prior study (Ref. 17). A deep ducted fan with a lengthy diffuser section is also viable in designs where the fan is embedded in the body of an aircraft such as the Phantom Swift (Ref. 1). The duct configuration from Figure 2 is the focus of this study, specifically to determine the effect the change in inlet geometry has on the performance of the system. The length L in Figure 2 is downplayed and is $4R$ in the computational model. This length ensures that in forward flight the flow entering the interior inlet is aligned parallel with the rotor plane. To fairly compare the performance of the two duct configurations, all exterior duct sections (black) are not considered. Therefore, only integrated thrust and moment values on the duct for the three interior sections mentioned above are included in this study.

The rotor used in this study is an APC 12x5.5 MR, a commercially available fixed pitch propeller commonly used on small unmanned aerial vehicles (Ref. 18). The rotor is hingeless and assumed sufficiently rigid that blade deformation was not included in the analysis. The actual rotor blade has a rounded tip, however for the purpose of the study a square tip was used.

This rotor is two bladed and the chord and twist along the span of the blade were measured and tabulated in Table 1. The airfoil sections were assumed to be a NACA 4412 at the root, an Eppler 63 at 20% span, and a Clark Y at the tip, using linear interpolation at any point in between.

Table 1 APC 12x5.5 Blade Geometry

Radial Position (r/R)	Local Chord (cm)	Geometric Twist (degrees)	Airfoil Sections
0	Hub	Hub	NACA 4412
0.1	1.605	20.8	Linear Interp.
0.2	2.393	32.5	Eppler 63
0.3	3.073	27.9	↑
0.4	3.195	21.5	
0.5	3.015	18.0	Linear
0.6	2.751	14.5	Interp.
0.7	2.413	11.0	↓
0.8	1.958	9.5	
0.9	1.455	8.0	
1.0	1.130	6.5	Clark Y

A blade tip to duct wall clearance of 0.1524 cm or 1% of the rotor radius was used in the model. The rotor is assumed to have zero sweep along the line connecting the 50% chord point of each airfoil section. The circular rotor hub is included in the CFD simulation and has a radius of 0.826 cm, resulting in a 5.4% root cutout.

The ducted rotor was simulated in hover as well as translational flight conditions of 10 m/s. The rotor speed was maintained at 4300 RPM regardless of flight condition and the ducted fan remained at 0° (nose level) pitch attitude. This ducted fan was not trimmed to any flight condition but the resulting lift, drag, pitching moment, etc. are calculated and reported for the prescribed rotor RPM and pitch attitude.

C. Computational Method

A three-dimensional transient solution to the RANS equations was determined using AcuSolve, a stabilized 2nd order (temporally and spatially) upwind finite element solver specifically designed for incompressible or weakly compressible

flows up to local Mach numbers of 0.8 (Ref. 19). The advancing rotor blade in this study saw freestream Mach numbers less than 0.23 when the ducted rotor translated at 10 m/s, therefore an incompressible solver was suitable. For modeling turbulence the Spalart-Allmaras RANS model was used. The Reynolds number for the duct, based on a typical axial speed of 10 m/s (average velocity induced by the rotor) and the height = $d + r = 0.26$ m, was approximately 1.66×10^5 . The Reynolds number for the blades based on the chord and the tangential speed at $0.75R$ for 4,300 RPM was approximately 9.19×10^4 . The flow at these Reynolds numbers is expected to be transitional for moderate angles of attack. However, given the effective angles of attack are rather large so that significant separation is anticipated and the incoming flow is likely to be unsteady, a turbulent approximation is a reasonable choice.

The computational domain is shown in Figure 3, an inflow with prescribed velocity and an outflow with zero pressure offset boundary were defined. Other boundaries of the control volume were set to far field which allowed flow to cross the boundary in either direction with no pressure offset. In the hover case, the inlet and outlet were also set to far field.

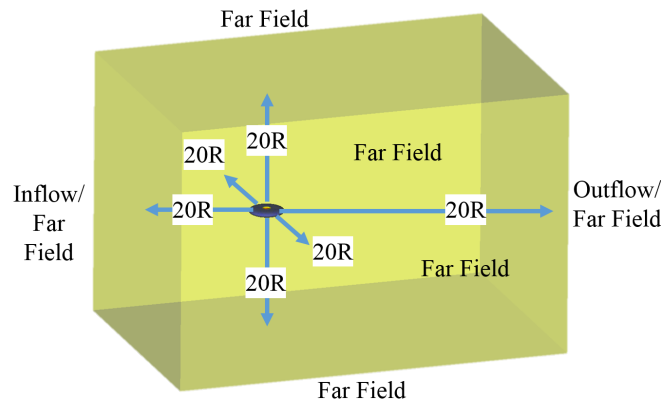


Fig. 3 Computational domain and boundary conditions for embedded duct model

A sliding mesh interface was employed to simulate full rotor revolutions in this study. The sliding mesh method requires two separate volumes inside the computational domain: one volume that rotates with respect to the inertial frame and one that remains stationary. These two volumes are coincident only along the sliding interface surface which passes information between the two volumes. Figure 4 shows the rotating volume (purple) and sliding interface along with the non-rotating volume. The rotating volume is a cylinder centered about the rotor hub; it has a radius of 15.32 cm and extends both above and below the rotor plane by 2.54 cm. The radius of this rotating volume is such that it ends in the middle of the tip gap clearance. The rotor radius is 15.24 cm, this results in 0.0762 cm inside the rotating volume between the rotor tip and the sliding interface and 0.0762 cm between the sliding interface and duct wall in the non-rotating volume.

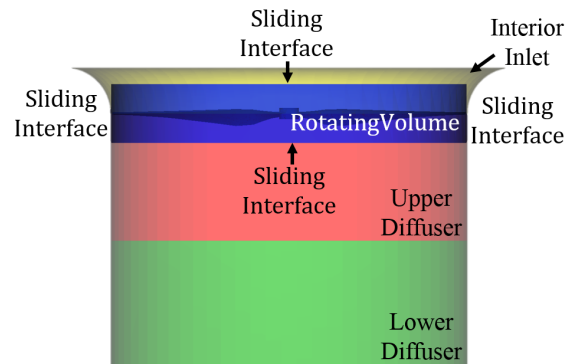


Fig. 4 Sliding interface between the non-rotating volume containing the duct and the rotating volume containing the rotor

The domain was discretized using a meshing software developed by Simmetrix (Ref. 20). The mesh was entirely comprised of unstructured tetrahedral elements. Surface mesh element size control was implemented on the surface of the blades ensuring a maximum element size 1/50th the blade chord. The elements on blade were refined by a factor of 10 \times in the leading (0-10% chord) and trailing edge (90-100% chord) of the blades, (compared to the elements along the remainder of the chord).

The surface of the duct was also discretized using an unstructured mesh. The size of the surface elements was set to 1/50th the length of the diffuser. Given the curvature of the interior inlet section the element size was reduced by 10 \times for this section of the duct. A second refinement region was established on the duct surface near the rotor plane ($\pm 0.1R$), the element size is locally reduced to 0.0254 cm; this is the same size as the elements on the rotor tip as shown in Figure 5.

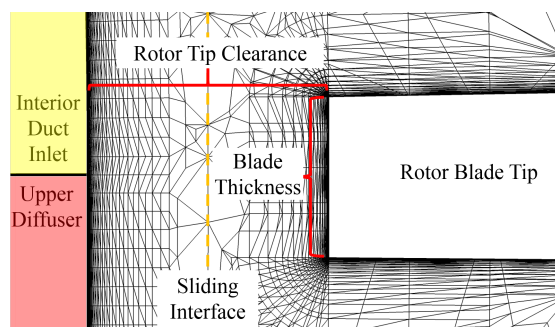


Fig. 5 Cut plane of ducted rotor mesh in the region between the rotor tip and duct wall from looking down the chord of the blade

On both the rotor and the duct a structured boundary layer mesh was employed. The first element height was set to ensure $y^+ \leq 1$ throughout, estimated using a flat plate at 78 m/s (the advancing blade tip speed). The mesh consisted of 41 million grid points in total with 28 million coming from the rotating volume and 13 million coming from the non-rotating volume.

A mesh refinement study was conducted by varying the following parameters: size of elements along the chord of the rotor, the leading/trailing edge reduction ratio, the aspect ratio of elements along the span of the rotor, the chordwise elements on the duct, the local element size near the rotor plane, the azimuthal element size on the duct, and the number of elements in the boundary layer. Each parameter was independently doubled in refinement, convergence was determined when the thrust changed by less than 1% from the previous setting. The values specified in this section are the results of this convergence study.

The rotor was simulated spinning at 4300 RPM for all flight conditions. All cases were run initially using large 10 $^\circ$ timesteps to let flow develop more quickly, then each simulation was restarted for additional revolutions at 1 $^\circ$ timesteps until convergence was achieved. The initial 10 $^\circ$ timesteps are possible without causing solution divergence due to the Streamline Upwind Petrov-Galerkin (SUPG) finite element method and Generalized α implicit time integration method which is known for suppressing high frequency disturbances and allowing solution stability with Courant–Friedrichs–Lewy (CFL) number > 1 (Refs. 21, 22).

Most runs were performed on 512 2.6 GHz Intel Xeon E5-2650 processors, part of the Center for Computational Innovations (CCI) at Rensselaer Polytechnic Institute. Meshing was completed using the higher memory 3.3 GHz Intel Xeon E5-2643 processor with 256 GB of system memory, also part of the CCI facility.

IV. Inlet Geometry Comparison

A prior study has closely examined the flow physics and performance of an isolated ducted rotor in hover and forward flight (Ref. 17). The following sections provide a comparison of the results in that study to the embedded ducted rotor configuration. The interior duct geometry, rotor geometry, rotor speed, flight speed, and nose-level pitch attitude are the same between both configurations. The difference in the exterior geometry of the ducts will change the flow conditions at the inlet of the duct and the performance of the system. The trade-offs in performance are examined in the following sections.

A. Hover Performance

The isolated and embedded duct configurations were analyzed in hover and no significant differences in performance were calculated. Both rotors produced approximately 3.4 N of thrust and required 43 W of power. The velocity magnitudes of the two configurations are compared in Figure 6 and Figure 7. These figures show in hover the inflow velocities and wake structure are very similar confirming the equal performance of the two configurations in hover.

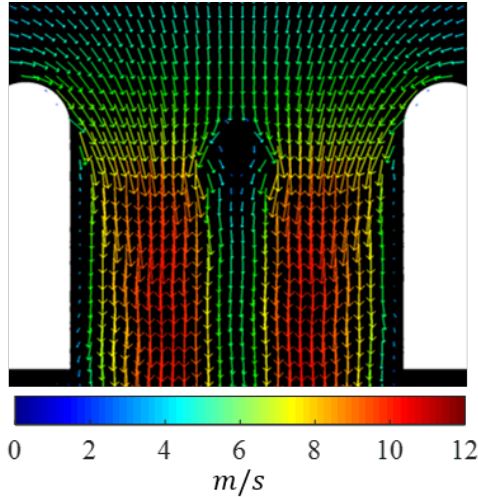


Fig. 6 Velocity vectors of flow through the isolated ducted rotor in hover

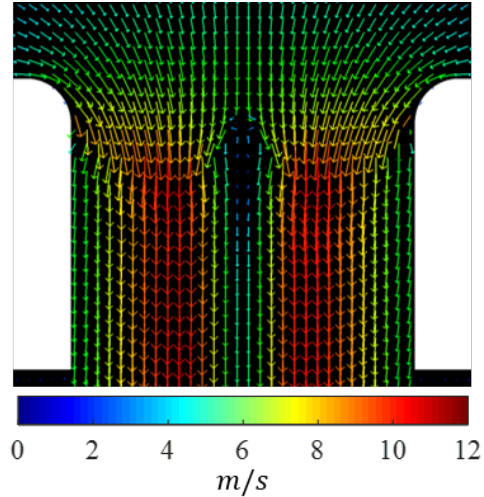


Fig. 7 Velocity magnitude of flow through the embedded ducted rotor in hover

B. Forward Flight Performance

For the the isolated and embedded duct configurations, an edgewise flight condition of 10 m/s was considered. As the ducted rotor in this study has zero nose down attitude, the duct interior behaves like the upper/lower of an airfoil where the angle of attack is determined by the relative freestream velocity and induced velocity of the rotor, as shown in Figure 8.

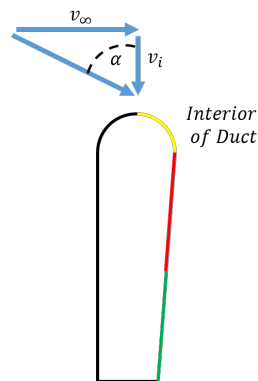


Fig. 8 Effective angle of attack on duct inlet due to freestream velocity and induced inflow

Since the freestream velocity (v_∞) is much larger than the induced velocity (v_i) at the inlet even at moderate flight speeds, the effective angle of attack (α) of the duct inlet is nearly 90° which places the forward section of the duct inlet in deep stall. At 10 m/s forward flight speed, flow separates off the duct inlet for both configurations resulting in an area of low pressure and vorticity in the region of separation (seen in Figure 9 and Figure 10).

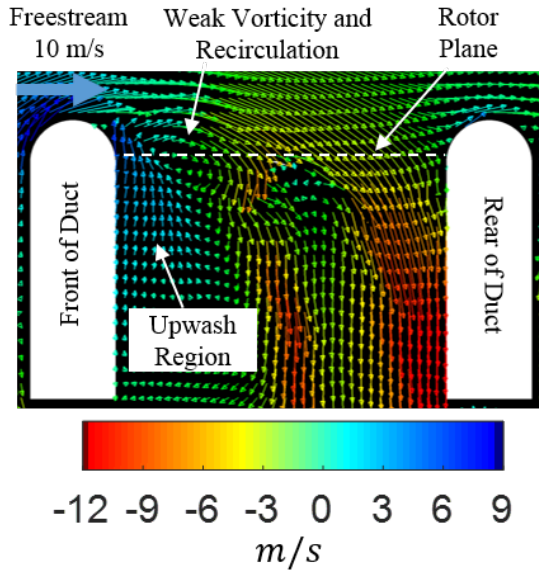


Fig. 9 Velocity vectors of flow inside isolated ducted rotor colored by axial velocity

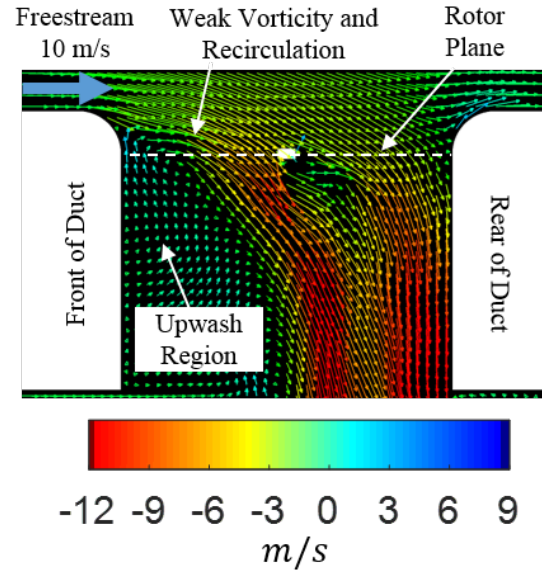


Fig. 10 Velocity vectors of flow inside embedded ducted rotor colored by axial velocity

For the embedded duct the incoming flow is aligned parallel to the rotor plane whereas flow travels up over the exterior portion of the inlet in the isolated case. This delays the separation point of the flow for the embedded ducted rotor. In Figure 9 the flow separates off the upstream duct inlet near the tallest point of the duct leading to a region of separation that extends nearly the entire front half of the rotor plane. Alternatively, Figure 10 shows the flow stays attached for part of the inlet and separates lower on the duct inlet (closer to the rotor plane) and the separation region only extends through the first quarter of the rotor plane. Along with the size of the separation region, the magnitude of the velocity vectors in Figure 9 and Figure 10 shows the strength of the vorticity and magnitude of the upwash at the front of the rotor plane is higher for the isolated duct configuration. Lastly, the rotor induces higher velocity at the rear of the disk for the embedded configuration. The following sections will explain how the observed flow physics of the two duct configurations affect the performance of the rotor and duct.

1. Rotor Aerodynamics

Analysis of the ducted rotors shows that the rotor experiences a unique flow phenomenon in forward flight due to the presence of the duct. The flow physics that affect the rotor performance will be investigated in this section.

Figure 11 and Figure 12 show that in edgewise flight the peak rotor thrust is generated at the front of the disk. This is unlike a fixed pitch open rotor where the highest lift is expected on the advancing side due to increased dynamic pressure. The flow separation region on the front inlet results in an area of recirculation near the rotor plane (Figure 9 and Figure 10). This induces an upwash through the rotor plane in the front portion of the disk. The cut plane in Figure 9 and Figure 10 is along the $\Psi = 0^\circ - 180^\circ$ line while the blades are at 90° and 270° . When the blade rotates through the front of the disk, it will see an upwash on the outboard sections. The upwash increases the effective angle of attack locally and ultimately produces more lift in this region. This is confirmed by the distribution shown in the disk plots of rotor thrust (Figure 11 and Figure 12). Note that the magnitude of the maximum thrust and disk area producing high lift is smaller for the embedded duct than the isolated duct. This is a result of the smaller separation region on the embedded duct and smaller magnitude of upwash through the rotor plane compared to the isolated duct.

In the disk plot of rotor thrust (Figure 11 and Figure 12) a lateral distribution is observed as well, with high thrust near the front of the disk biased slightly to the retreating side. As the blade enters the upwash region near $\Psi = 120^\circ$ (Figure 13), it interacts with the slow moving upwash and sweeps it along with the blade in the direction of rotation. The top row shows the isolated ducted rotor and the bottom row shows the embedded configuration. The black line represents the line of zero axial velocity. All area on the red side of this line corresponds to flow traveling down through the rotor and into the diffuser section of the duct, all area on the blue side of this line corresponds to upwash through the rotor plane. As the blade cuts through this region the upwash stacks up along the span of the blade moving more lift

inboard. Figure 13 (b) and (e) shows the blades at $\Psi = 0^\circ$ and $\Psi = 180^\circ$. At this point, the outboard 70.8% of the blade at the front of the disk sees relative upwash in the isolated configuration compared to the outboard 58.3% for the embedded case. This upwash increases the lift of the blades at these spanwise locations and corroborates with the blade elemental thrust distribution (Figure 11 and Figure 12) at $\Psi = 180^\circ$.

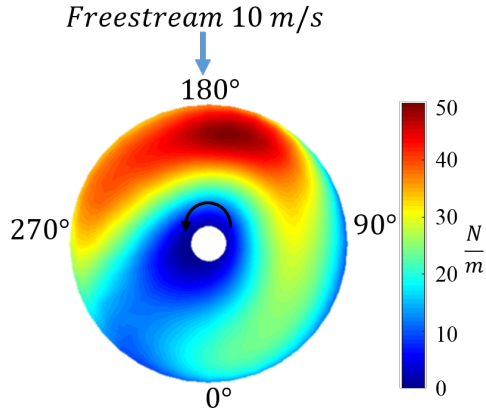


Fig. 11 Blade elemental thrust of the isolated ducted rotor at 10 m/s forward flight conditions

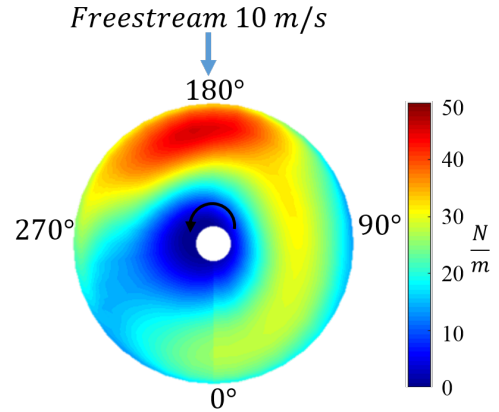


Fig. 12 Blade elemental thrust of the embedded ducted rotor at 10 m/s forward flight conditions

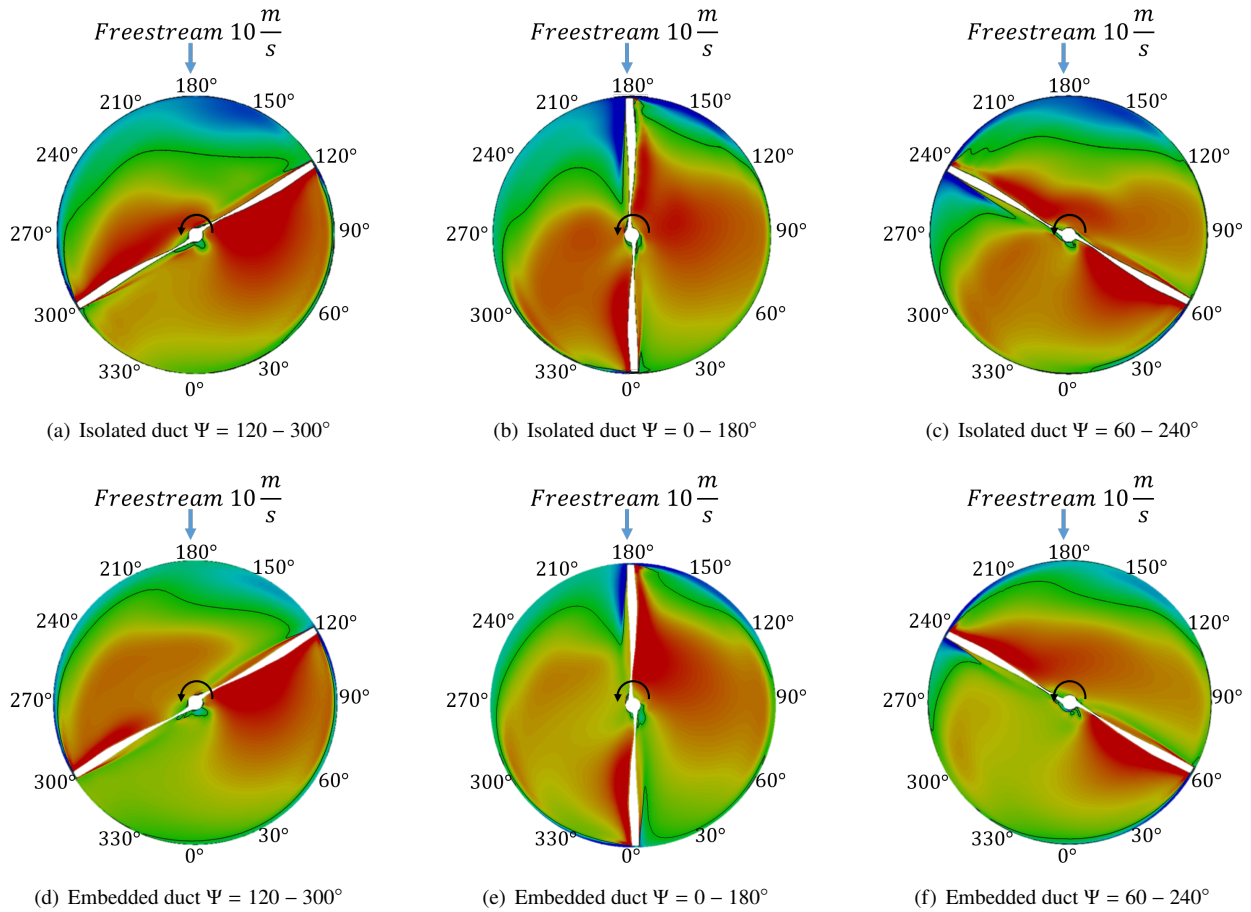


Fig. 13 Axial velocity through the rotor plane of the ducted rotor translating at 10 m/s as the rotor passes through the separation region. The isolated duct is shown in a, b, and c and the embedded duct in d, e, and f

The disk plots of blade elemental drag in Figure 14 and Figure 15 show the difference of the two duct configurations at 10 m/s forward flight speed. These plots show that the drag on the rotor is highest near the midspan on the advancing side. This spanwise location has the highest geometric pitch and largest chord which causes the high drag. This is also the azimuthal location that sees the highest dynamic pressure due to the freestream velocity. Although the front of the disk sees the highest lift, the upwash in that region reduces the induced drag on the blade, which in turn limits the total rotor drag. The larger upwash velocity on the isolated duct configuration accounts for the larger drag reduction at the front of the disk.

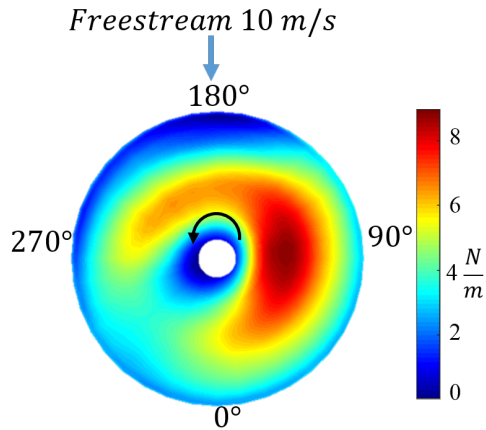


Fig. 14 Blade elemental drag of the isolated ducted rotor at 10 m/s forward flight conditions

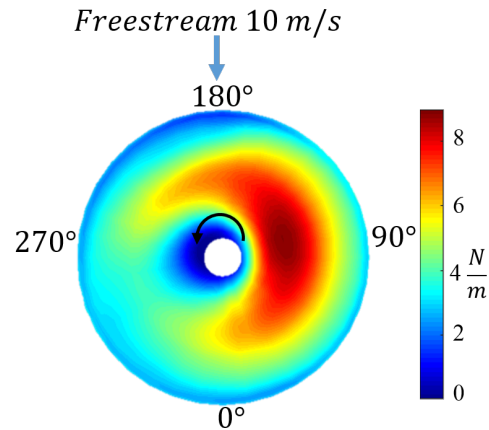


Fig. 15 Blade elemental drag of the embedded ducted rotor at 10 m/s forward flight conditions

The overall steady forces and moments on the ducted rotors in forward flight are averaged over a revolution and will be reported in a subsequent section focused on the overall performance metrics.

2. Duct Aerodynamics

The duct significantly contributes to the full vehicle integrated forces and moments. The primary forces acting on the duct are the thrust and drag (H-force), and the primary moment on the duct is nose-up pitching. All moments presented in this study are taken about the rotor hub. The pitching moment arises from azimuthal asymmetry of the thrust and H-force around the duct on the inlet and diffuser sections. The duct forces and moments presented in this section are the steady loads on the duct averaged over one rotor revolution.

Figure 16 and Figure 17 show the azimuthal distribution of the duct thrust (defined as total force acting vertically in the +Z direction), at 10 m/s forward speed for the isolated and embedded duct respectively. In forward flight, thrust on the duct is produced primarily on the front inlet with no significant contribution from the diffuser section. Even with the front half of the duct behaving like an airfoil in deep stall and the flow separating off the inlet, the duct inlet produces a significant amount of lift. Both the isolated and embedded duct have similar thrust distributions but the isolated duct produces more total thrust overall.

A secondary effect is the rotor swirl biasing the upwash and duct inlet separation region slightly to the retreating side of the inlet. In the separation region, the duct inlet sees higher gauge pressure than where flow stays attached and in turn, the thrust produced by this portion of the inlet is reduced. This is verified by the duct thrust distribution plots in Figure 16 and Figure 17 where the thrust peaks near $\Psi = 135^\circ$ then drops off on the front of the duct.

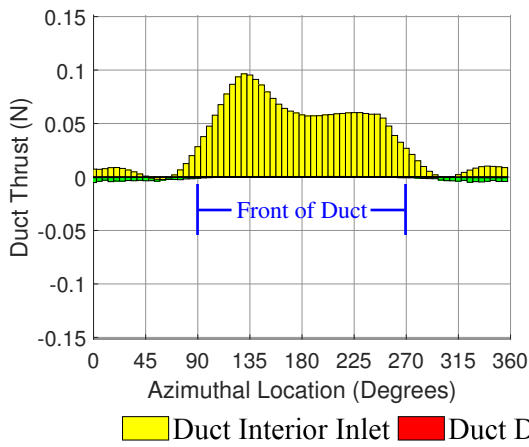


Fig. 16 Azimuthal breakup of isolated duct thrust at 10 m/s forward flight conditions averaged over one rotor revolution

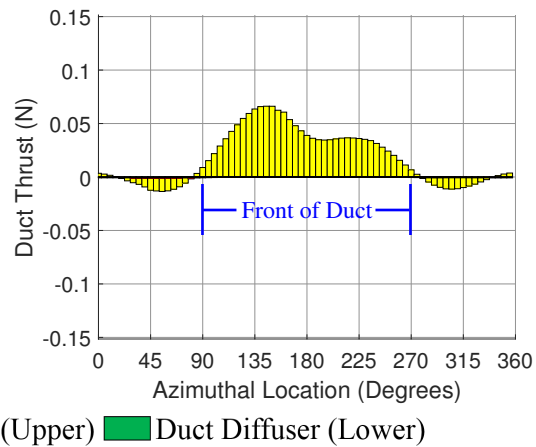


Fig. 17 Azimuthal breakup of embedded duct thrust at 10 m/s forward flight conditions averaged over one rotor revolution

Figure 18 and Figure 19 show the azimuthal distribution of H-force on the duct. In forward flight duct drag comes primarily from two sources, the suction on the front inlet and the ram pressure from the stagnation of the freestream on the rear of the duct (primarily on the upper diffuser). The first source of drag on the duct comes from the radial component of suction on the inlet. At the front of the duct this component acts in the direction of aircraft drag. At the front of the duct there is a key difference between the two duct configurations. For the isolated duct the upper and lower diffuser are small contributors to duct H-force due to the low pressure in the region of separated flow. This suction acting on the front of the diffuser has a radial component in the drag direction. On the other hand, the front diffuser sections in the embedded configuration see a high pressure that results in propulsive force on the duct, partially canceling the drag on the front inlet. As previously noted, the separation region on the embedded duct is smaller resulting in less suction acting on the diffuser sections. The high pressure acting on the front of the diffuser comes from the high pressure on the lower surface of the blades interacting with the diffuser at $2/\text{rev}$. The interaction between the blade and duct will be further explained in the vibratory loads section but the steady component of load due to blade passage results in a net propulsive force on the front of the diffuser.

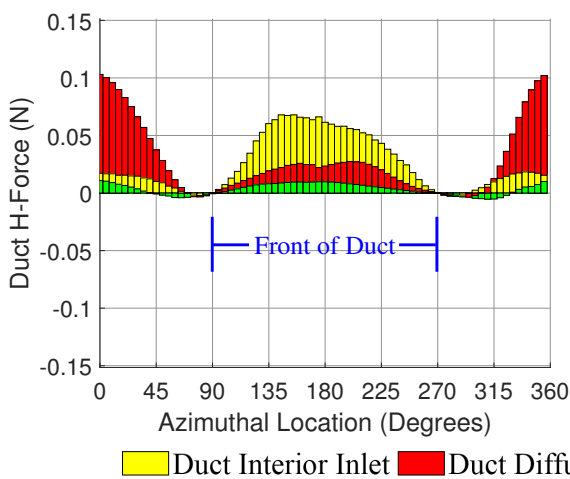


Fig. 18 Azimuthal breakup of isolated duct H-force at 10 m/s forward flight conditions averaged over one rotor revolution

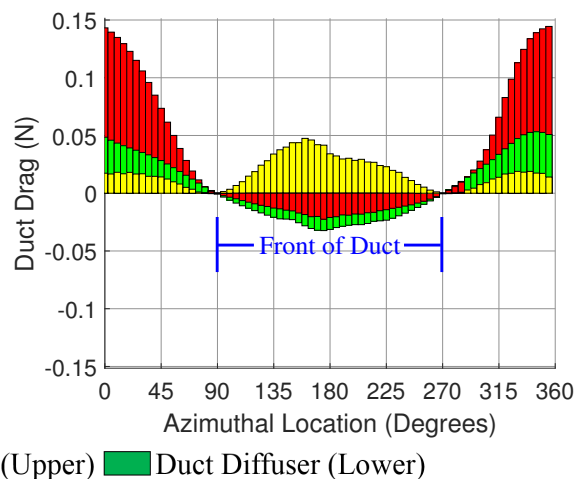


Fig. 19 Azimuthal breakup of embedded duct H-force at 10 m/s forward flight conditions averaged over one rotor revolution

The other major contributor to duct H-force comes from the ram pressure at the rear of the duct as seen in Figure 20 and Figure 21, corresponding to 10 m/s forward flight speed. The rotor induces an inflow which attempts to turn the flow 90° from its freestream velocity to one aligned with the Z (vertical) axis of the duct. However, when the induced inflow velocity is much lower than the freestream velocity the rotor only manages to turn the air slightly downward. This flow collides with the rear of the duct near and below the rotor plane. The location of this stagnation area vertically on the duct will depend on the magnitude of the rotor induced velocity relative to the freestream velocity. The stagnation area on the rear of the embedded duct is lower on the diffuser and stronger in magnitude compared to the isolated duct accounting for the increase in H-force (Figure 18 and Figure 19) in that region. The increase in strength and lower location of the stagnation region on the embedded configuration comes from the incoming flow being parallel to the rotor plane. The velocity vectors in Figure 9 and Figure 10 show the difference in the flow above the rotor plane behaves differently in the front half of the duct. In the isolated configuration, some of the flow travels up over the exterior portion of the inlet giving these fluid particles an upward trajectory shown in Figure 9. Conversely, the velocity vectors in the same region of Figure 10 have a downward axial component, thus more flow colliding with the rear of the diffuser in the embedded configuration. The stronger and lower stagnation region on the embedded configuration explains the increase in H-force of the rear diffuser sections of the embedded configuration (Figure 19).

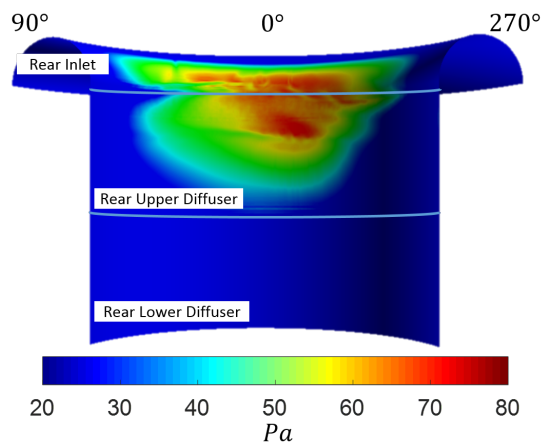


Fig. 20 Pressure on isolated duct surface looking at rear half of duct for 10 m/s forward flight case. Stagnation area observed near $\Psi = 0^\circ$ is large source of drag

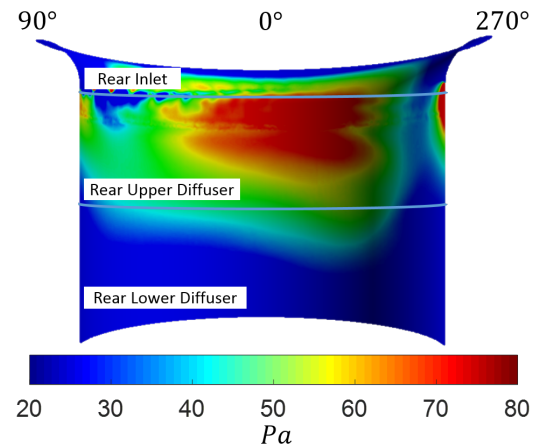
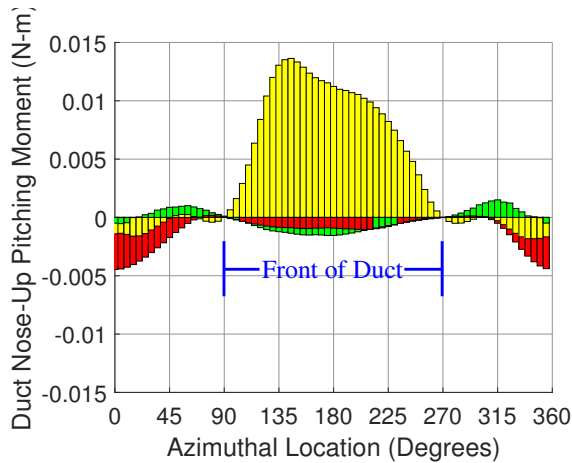


Fig. 21 Pressure on embedded duct surface looking at rear half of duct for 10 m/s forward flight case. Stagnation area observed near $\Psi = 0^\circ$ is large source of drag

Finally, Figure 22 and Figure 23 shows the generation of pitching moment around the duct at 10 m/s. The pitching moment comes predominantly from the duct thrust at the front inlet. Since the inlet of the embedded duct produces less lift than the isolated duct, the pitching moment is also reduced. The H-force on the duct is a secondary contributor.

The duct H-force (Figure 18 and Figure 19) also affects the total pitching moment taken about the rotor hub. The azimuthal location and height relative to the rotor plane dictate the direction of the induced pitching moment. The propulsive H-force on the front inlet of the embedded duct induces a nose up moment about the rotor hub. However, the positive H-force on the diffuser section at the rear of the duct, being below the rotor plane, induces a nose down moment. While the H-force on the rear diffuser is larger than or equal to the duct thrust generated at the front inlet, the small moment arm between the drag sources and the rotor plane reduces their net effect on generation of steady pitching moments.

For both duct configurations the steady component of duct side force and rolling moment were small, thus an azimuthal breakup of the generation of these forces and moments is not presented.



■ Duct Interior Inlet
 ■ Duct Diffuser (Upper)
 ■ Duct Diffuser (Lower)

Fig. 22 Azimuthal breakup of isolated duct H-force at 10 m/s forward flight conditions averaged over one rotor revolution

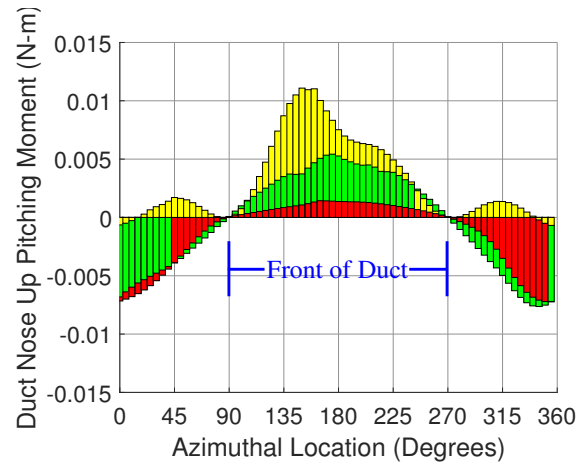


Fig. 23 Azimuthal breakup of embedded duct H-force at 10 m/s forward flight conditions averaged over one rotor revolution

3. Ducted Rotor Performance

In addition to identifying the major sources for the generation of forces and moments (thrust, H-force, and pitching moment), this study also looked at these behaviors at the full aircraft level by integrating around the full azimuth and time averaging over a full revolution then comparing the results of the two duct configurations. The following results present the full aircraft behavior at 10 m/s. Figure 24 shows the difference in thrust on the rotor and duct surfaces for the isolated and embedded ducted rotors.

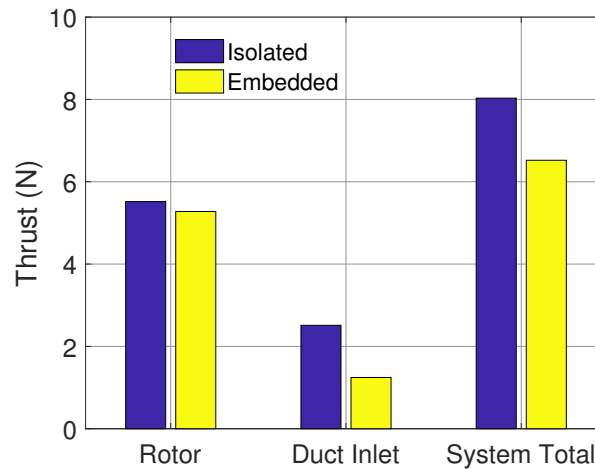


Fig. 24 Thrust of rotor and inlet compared for isolated and embedded duct at 10 m/s

In forward flight the rotor thrust produced with the embedded duct was 4.4% lower than the isolated duct while the duct inlet produced 50.4% lower thrust in the embedded configuration. With the rotor being the dominant contributor to the total thrust (68.7% and 80.1% for the isolated and embedded configurations respectively), the total thrust of the embedded ducted rotor configuration is calculated to be 18.8% lower than the isolated ducted rotor.

The steady H-force for the isolated and embedded duct at 10 m/s, shown in Figure 25, indicates that the rotor is a

negligible contributor. From the previous section looking at the duct contributions to H-force (Figure 18 and Figure 19), most of the drag generated by the inlet comes from the suction at the front of the duct. The H-force on the upper diffuser comes primarily from the ram drag as the freestream flow stagnates on the rear of the duct. When comparing the embedded duct to the isolated, the inlet produces less H-force but more ram pressure on the rear diffuser produces a higher H-force. The latter is, in turn, negated slightly by the propulsive force on the upper diffuser at the front. Overall, the reduction in H-force on the inlet is the most significant difference between the two duct configurations and the embedded duct has 6.3% less total H-force.

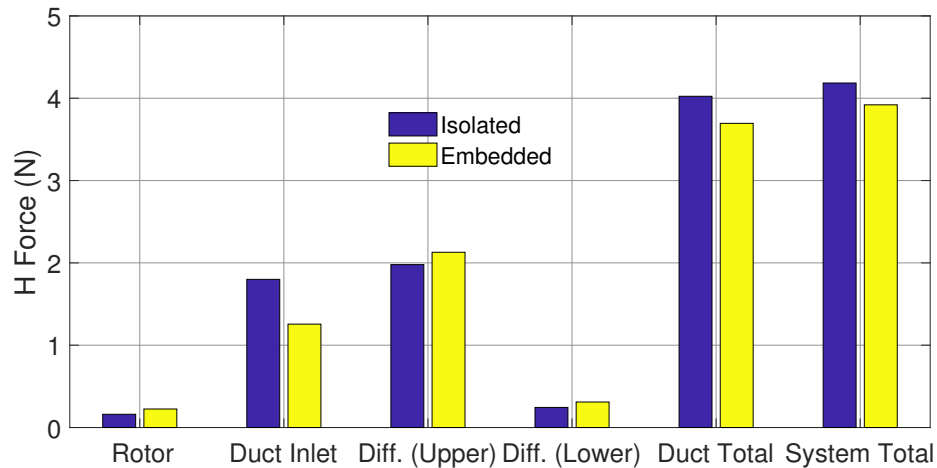


Fig. 25 H-force of rotor and duct interior compared for isolated and embedded configurations at 10 m/s

There difference in rotor power is negligible between the two duct configurations (45.4 Watts for the isolated configuration and 46.6 Watts for the embedded configuration) showing the rotor power is almost entirely dependent on the rotor RPM. However, the L/D_E is 17.3% for the embedded configuration as a result of the slight reduction in thrust and H-force.

Figure 26 shows the comparison of pitching moment for the two duct configurations. The thrust on the front inlet (Figure 16 and Figure 17) and the upwash region increasing the rotor blade's effective angle of attack at the front of the disk (Figure 11 and Figure 12) explains the duct inlet and rotor nose up pitching moment. The rotor contributes 43.8% and 42.5% of the total nose-up pitching moment for the isolated and embedded configurations respectively at 10 m/s. The upper and lower diffuser sections produces a nose down pitching moment due to the ram drag at the rear of the duct, but this only partially negates the nose up pitching moment from the inlet. Note that the reduction in peak rotor thrust, and inlet thrust over the front of the disk, and increase in diffuser H-force due to ram drag, all contribute to a significantly weaker nose-up pitching moment on the embedded ducted rotor design. The embedded ducted rotor has a 47.4% lower nose-up pitching moment compared to the isolated ducted rotor.

Finally, the steady side force and accompanying roll moment from both duct configurations were observed to be negligible compared to the dominant forces and moments of the system (thrust, H-force, and pitching moment); the calculated values are at the limit of the accuracy level of this study.

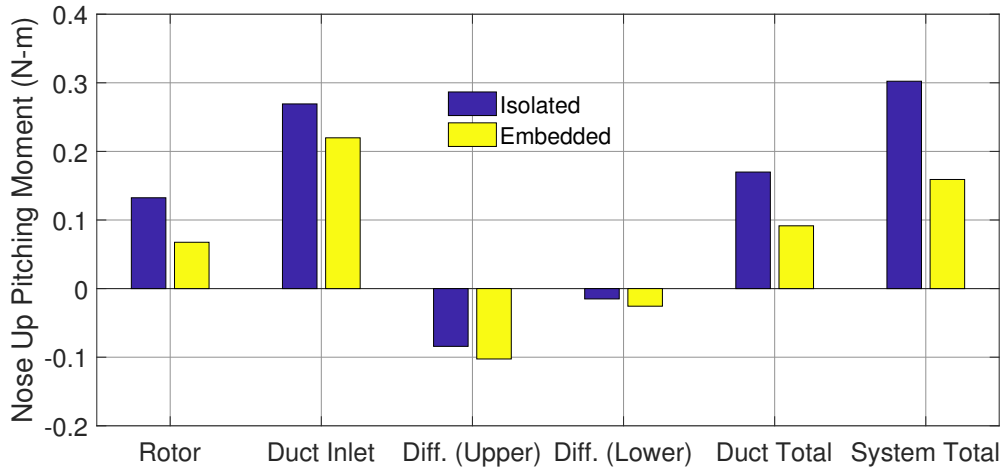


Fig. 26 Pitching moment of rotor and duct interior compared for isolated and embedded configurations at 10 m/s

C. Vibratory Loads

In addition to the steady vehicle loads, the vibratory loads associated with the blade passage frequency were also analyzed as part of this study. Both the rotor and the duct are sources of vertical and in-plane vibrations. The rotor vertical and in-plane vibrations come from azimuthal variation in the blade root vertical shear S_z and chordwise shear S_x . Figure 27 shows the blade root vertical shear at 10 m/s forward speed for both the isolated and embedded duct configurations. The S_{z2p} of each blade contributes to the rotor hub 2/rev vertical vibratory loads in the non-rotating system while the S_{z1p} vibrations are canceled at the hub for a two-bladed rotor. Although the peak-to-peak variation in S_z loads is significantly greater for the isolated duct case (consistent with the larger lift at the front of the rotor disk seen in Figure 11 and Figure 12), the 2/rev component is only about 6.7% larger. Figure 28 shows the blade chordwise (drag) shear loads over one revolution. Note that the magnitude of S_{x1p} vibration, is the source of the rotor hub in-plane vibrations

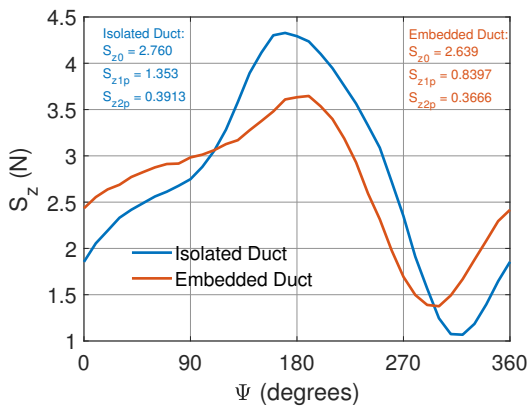


Fig. 27 Blade root vertical shear forces over one revolution at 10 m/s for the isolated (blue) and embedded (orange) duct configurations

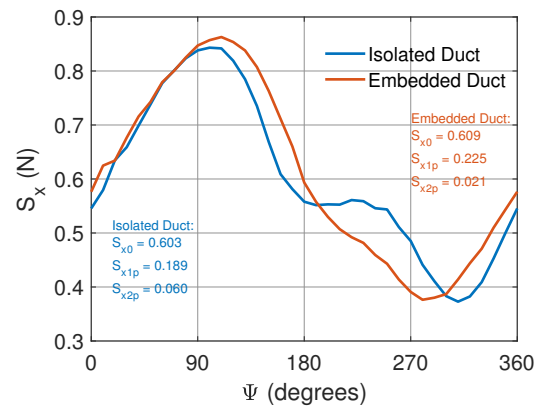


Fig. 28 Blade root chordwise shear forces over one revolution at 10 m/s for the isolated (blue) and embedded (orange) duct configurations

The duct is also a significant contributor to the in-plane vibrations. Due to the very small clearance between the rotor tip and duct wall the high pressure on the lower surface near the blade tip and the low pressure on the upper surface near the blade tip exert local forces on the duct. Figure 29 shows the pressure on the surface of the duct immediately adjacent to the blade tip at various azimuthal locations for the isolated and embedded duct designs. A component of these forces on the duct inlet act in the vertical direction resulting in a small duct contribution to vertical vibrations (Figure 32).

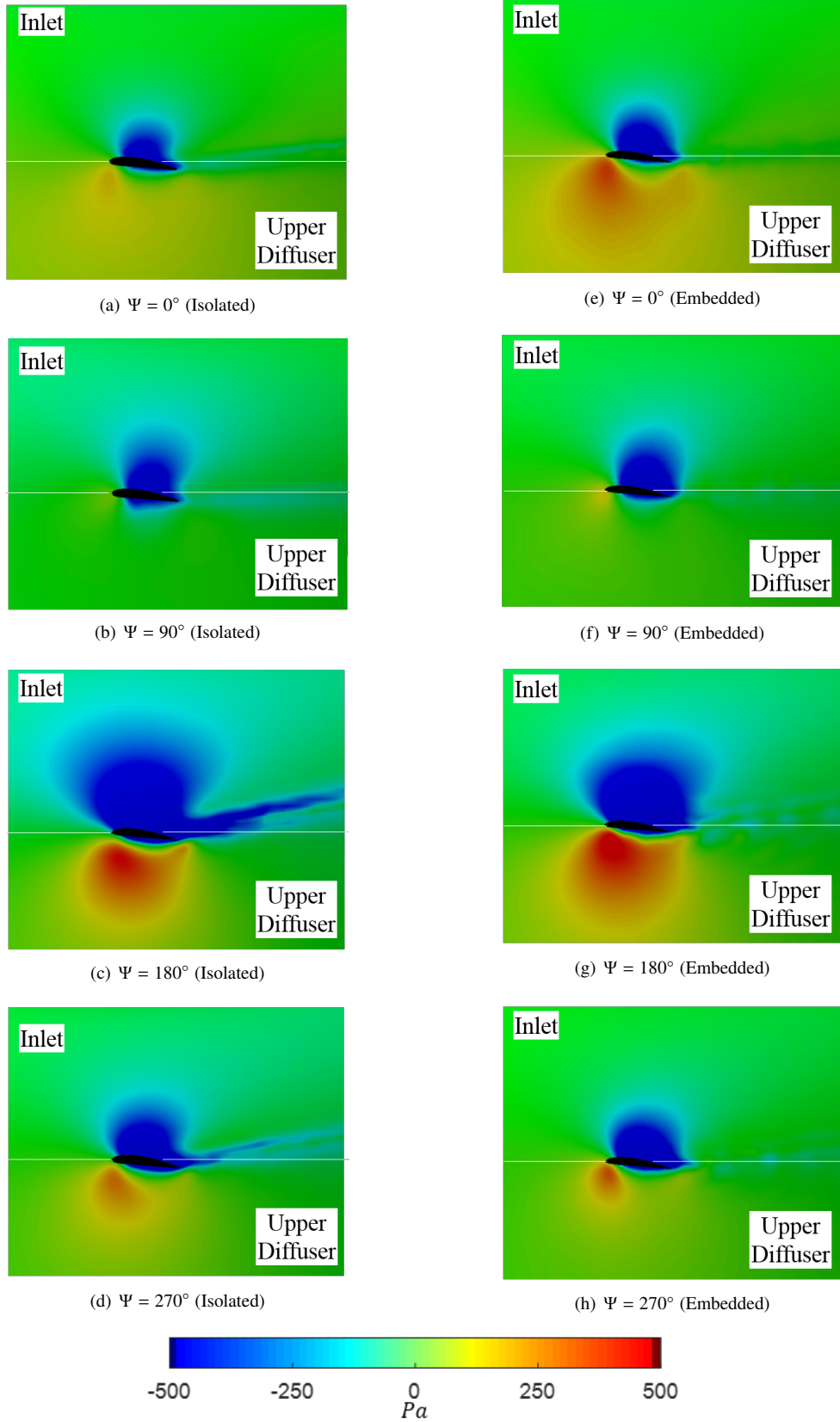


Fig. 29 Pressure contours on duct inlet and upper diffuser adjacent to rotor tip at various azimuth positions for the isolated (a,b,c,d) and embedded (e,f,g,h) duct configurations

Note in Figure 29 the suction on the duct above the blade tip inlet and the higher pressure on the duct wall below the rotor tip (upper diffuser) at any azimuthal location do not cancel, resulting in a net force that contributes to in-plane vibratory loads. Additionally, the magnitude of the in-plane H-forces generated at the front of the disk ($\Psi = 180^\circ$ on Figure 29) are much higher than those at the rear (due to the higher lift generated by the rotor blades at the front), creating further azimuthal variation in in-plane forces on the duct. The suction above the blade and high pressure below the blade also induces a net moment about the rotor plane.

Figure 30 and Figure 31 show the instantaneous unsteady H-force and pitching moment for the duct components for both configurations at the 10 m/s. Positive F_x represents force in the drag direction and positive M_y represents a nose up pitching moment. These figures show the instantaneous vibratory loads (the steady loads have been removed) when the blades begin at 0° and 180° . For the F_x vibratory loads, the inlet and upper diffuser are 180° out of phase, this comes from a low pressure suction acting on the inlet while a high pressure acts on the upper diffuser. For the isolated duct, the upper diffuser is the primary contributor to the H-force vibrations, for the embedded configuration the magnitude of the unsteady loads on all portions of duct become smaller. Figure 29 shows that the suction region above the blade is stronger and affects a larger area than the high pressure region below the blade. However, the curvature of the inlet breaks the force exerted by this pressure into an in-plane component (shown in Figure 30) and a vertical component. The upper and lower diffuser vibratory loads are in phase. The high pressure causes an outward force on the upper diffuser and this effect carries to the lower diffuser. The magnitude of the force on the lower diffuser is reduced because it is further from the source of the high pressure. From the pitching moment analysis, all components of the duct are in phase as the suction acts above the rotor plane while the pressure acts below the rotor plane. All three duct interior components induce vibrations of similar magnitudes. While the lower diffuser sees smaller in-plane vibratory loads than the upper diffuser, it has a longer lever arm to the rotor hub, increasing its effect on moment induced vibrations. The duct inlet is not largely separated from the rotor plane in the vertical direction, however, the curvature of the inlet increases its contribution to moment vibrations. When the suction from the top of the blade acts on the inlet the resultant force is normal to the surface, one component in the radial in-plane direction and the other component in the vertical direction. This vertical component of the force has the radius of the duct acting as a lever arm and this accounts for the pitching and rolling moment vibrations induced by the duct inlet. Just as the F_x vibrations, the magnitude of the M_y vibrations on the embedded duct configuration are smaller than the isolated ducted rotor.

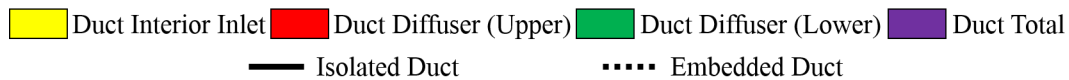
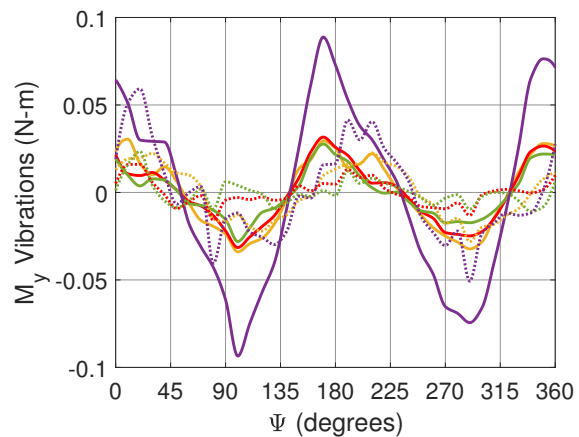
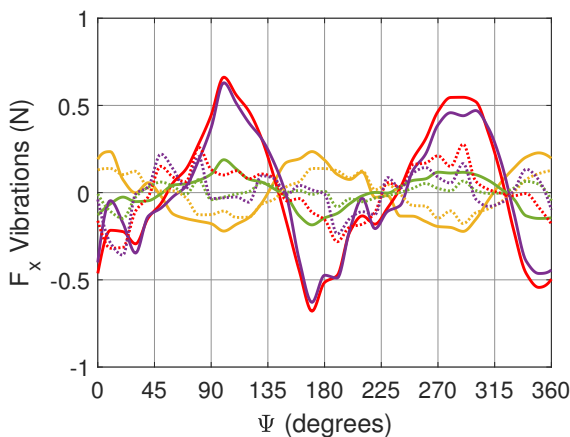


Fig. 30 Instantaneous unsteady H-force on duct components for 10 m/s forward flight case when the advancing blades starts at 0° and moves around the azimuth

Fig. 31 Instantaneous unsteady pitching moment on duct components for 10 m/s forward flight case when the advancing blades starts at 0° and moves around the azimuth

Comparing the isolated and embedded ducts, there is less longitudinal and lateral discrepancy between the pressure regions acting on the duct in the case of the embedded configuration. This is corroborated by the disk plots of rotor

thrust (Figure 11 and Figure 12) as the magnitude of these pressure regions is dependent on the local lift produced by the blade. Figure 12 showed less azimuthal variation in thrust produced by the rotor in the embedded duct compared to Figure 11 and the isolated duct, which explains why there is less azimuthal variation in the pressure acting on the duct in the embedded configuration.

The vibration magnitudes were examined in forward flight at 10 m/s. The contribution of each duct surface was analyzed separately and the full duct is the vectorial summation of all the interior surfaces. Lastly, the vibratory signals of the duct and rotor were the summed vectorially to assess the vibratory loads at the full aircraft level.

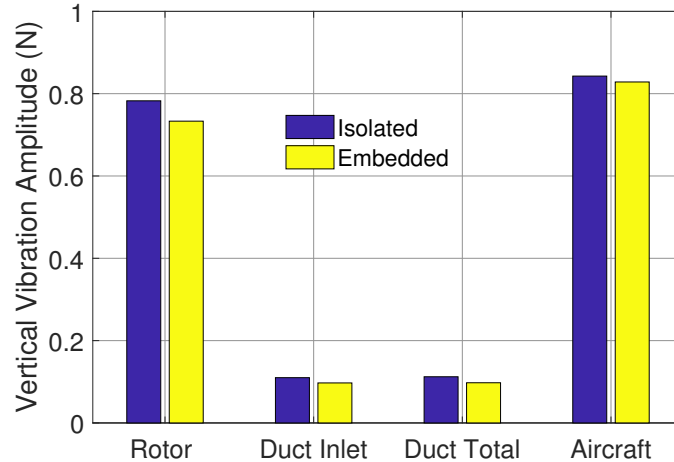


Fig. 32 Rotor and duct contributions to magnitude of vertical vibrations at 10 m/s

Figure 32 shows the magnitude of the 2/rev vertical vibrations for the isolated and embedded duct configurations. The rotor is the largest contributor to total aircraft vertical vibrations (92.9% and 88.5% at 10 m/s for the isolated and embedded ducts respectively). The duct inlet is the only duct surface that significantly contributes to the vertical vibrations. The vertical vibratory loads from the rotor are 14.1% of the isolated ducted rotor steady thrust and 13.9% of the embedded ducted rotor steady thrust at 10 m/s. With the rotor being the dominant contributor to vertical vibrations, the slight reduction in the S_{z2p} (Figure 27) for the embedded duct results in a small reduction in total aircraft vertical vibrations.

While the side force and rolling moment were negligible in their steady load contributions, the vibratory loads are substantial. Figure 33 and Figure 34 show that the in-plane vibratory loads in the longitudinal and lateral directions and have significant magnitude. For the in-plane vibratory loads on the isolated duct, the upper diffuser is the largest contributor and the entire duct contributes approximately 65% and 75% of the total longitudinal and lateral vibrations respectively. For the full isolated ducted rotor, the amplitude of the longitudinal in-plane vibration is 15.3% of the steady total H-force load. However, the embedded duct was able to significantly reduce the magnitude of the longitudinal and lateral vibrations on the entire duct. This in turn results in a reduction of the full aircraft longitudinal vibrations by 55.5% and 57.6% for the full aircraft lateral vibrations.

Similarly to the in-plane vibrations, the vibrations induced by the pitching moment (Figure 35) and rolling moment (Figure 36) are comparable in magnitude when analyzed at the 10 m/s. Figure 35 and Figure 36 show the rotor is the largest contributor to the moment induced vibrations (67% of the pitching and 65% of the rolling for the isolated duct). The magnitude of the full aircraft level isolated ducted rotor pitching moment vibrations are over 61.5% of the steady total pitching moment at 10 m/s. The embedded duct configuration significantly reduces the pitching and rolling moment induced vibrations on both the rotor and duct, reducing the full aircraft pitching moment vibrations by 57.0% and rolling moment vibrations by 55.3%. The magnitude of the full aircraft pitching moment vibrations on the embedded duct configuration is still 50.3% of the steady pitching moment but the steady component is also reduced by using the embedded duct configuration (Figure 26).

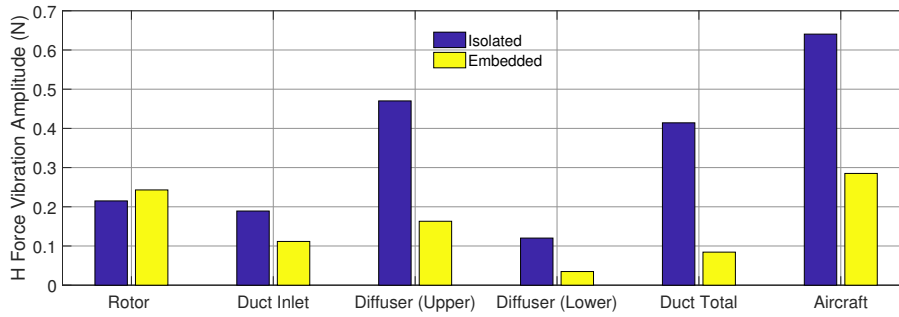


Fig. 33 Rotor and duct contributions to magnitude of longitudinal vibrations at 10 m/s

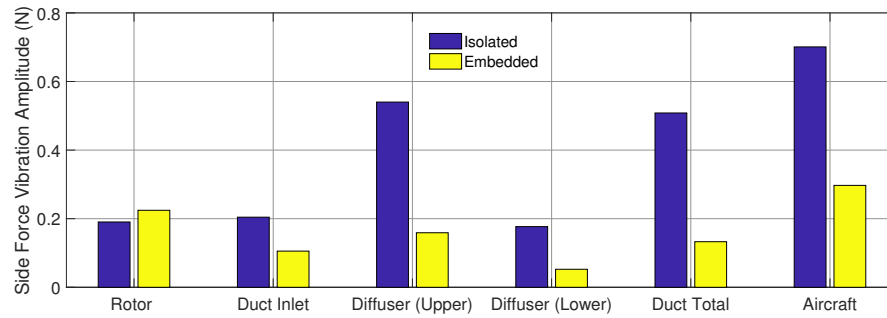


Fig. 34 Rotor and duct contributions to magnitude of side force vibrations at 10 m/s

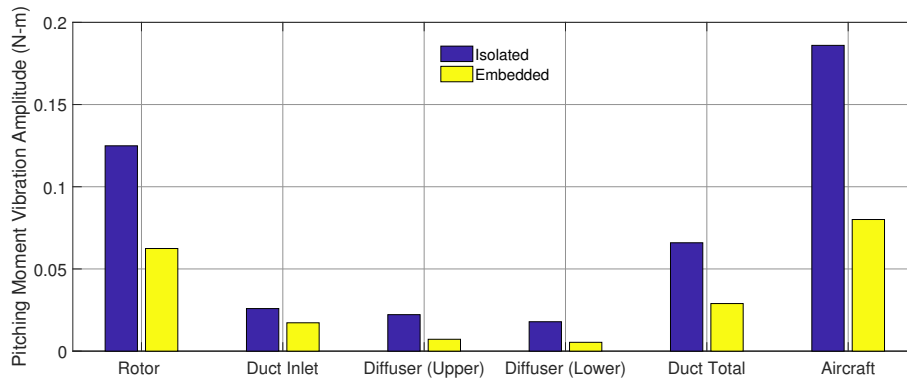


Fig. 35 Rotor and duct contributions to magnitude of pitching moment vibrations at 10 m/s

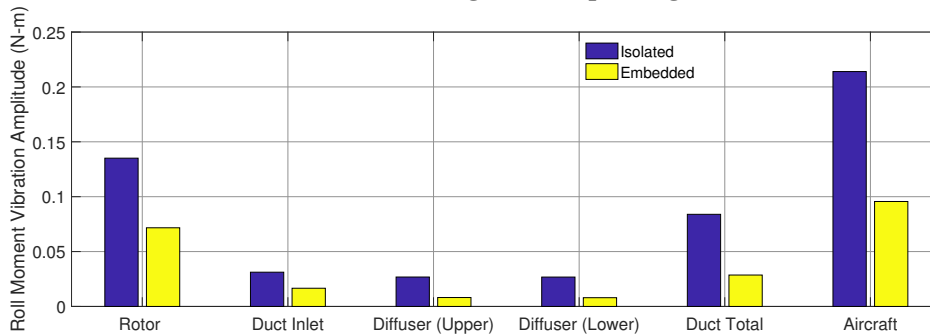


Fig. 36 Rotor and duct contributions to magnitude of rolling moment vibrations at 10 m/s

V. Conclusions

Using a three dimensional RANS CFD model, an isolated and embedded ducted rotor were simulated with a sliding mesh to analyze its behavior in hover and forward flight conditions given zero nose down attitude. This study examined the rotor and interior sections of the duct and determined the influence of each component on the performance, and provides a comparison between the two configurations. A detailed examination of the flow physics was used to understand the differences in the ducted rotor behavior due to different inlet geometries. The dominant steady forces and moments were analyzed as well as the vibratory loads on the ducted rotor system. The complex flow phenomena and rotor-duct interactions are explained as they pertain to the performance. While no significant differences were observed between the configurations in hover, the 10m/s cruise simulations presented in detail in this paper indicated significant differences between the two configurations in forward flight.

Specifically, the isolated duct configuration has a larger region of flow separation at the front than the embedded ducted rotor where the incoming flow is more aligned with the rotor plane. The larger separation region on the isolated ducted rotor induces a higher upwash velocity at the front of the rotor disk plane while the embedded ducted rotor induces a higher downwash velocity on the rear of the disk.

For the rotor, the highest thrust is produced at the front of the disk where the upwash increases the effective angle of attack of the blades, resulting in a rotor nose up pitching moment. The longitudinal variation in rotor thrust is reduced for the embedded rotor, in turn reducing the rotor nose up pitching moment by 49.0%. Unlike the maximum thrust which is seen at the front of the disk, the maximum rotor drag is observed on the advancing side. At the front of the disk although the lift is the highest the upwash reduces the induced drag, thereby limiting the total drag. The maximum drag on the advancing side is observed in the mid-span region rather than the outboard sections due to the high twist and taper ratio of the blade. For both duct configurations, the rotor is the dominant contributor to total thrust (68.7% and 80.9% for the isolated and embedded configurations respectively) and the induced power is not significantly affected by the inlet geometry. Lastly, the rotor is a small contributor to the total H-force providing less than 6% of the total for both configurations.

With regards to the duct, both configurations produce the majority of the thrust on the front inlet, though the embedded duct produces 50.4% less thrust than the isolated. The duct H-force comes predominantly from a combination of a component of the suction on the front inlet and ram pressure on the rear diffuser. The embedded duct produces less drag on the front inlet with blade passage further producing a small propulsive force on the front diffuser. However, the rear diffuser of the embedded configuration produces a larger H-force due to the stronger stagnation region. The net result is an 8.2% reduction in duct H-force for the embedded configuration. The duct nose-up pitching moment is reduced by 46.1% for the embedded configuration due to decreased thrust on the front inlet as well as increased H-force on the rear diffuser (which increases the nose-down pitching moment contribution).

The vertical vibrations of both duct configurations come primarily from the rotor. The magnitude of the 2/rev rotor vertical vibrations are reduced by 6.3% for the embedded configuration. The local pressure on the duct walls due to blade passage produces in-plane vibrations at the blade passage frequency. The magnitude of these vibrations, being tied to the instantaneous thrust produced by the nearby blade tip, are reduced for the embedded duct, where the rotor has less azimuthal thrust variation. The total H-force and side force vibrations are 56% and 58% lower respectively for the embedded duct configuration. The reduction in azimuthal thrust variation also significantly reduces the rotor pitching and rolling moment vibrations by 57% and 55% respectively for the embedded configuration.

VI. Acknowledgments

The authors would like to thank Rensselaer Polytechnic Institute and the Center for Computational Innovations. The findings from this study are only possible thanks to the availability of their computing resources and dedicated staff that maintain the network and hardware.

References

- [1] Ziegenbein, P., "PhantomSwift Quad-Ducted Rotor Aircraft Configuration Development," *American Helicopter Society 72nd Annual Forum, West Palm Beach, FL*, 2016.
- [2] Tatro, J., Yoeli, R., and Samples, D., "X-Hawk: Transformational Mobility for the Urban Warfighter," *American Helicopter Society 62nd Annual Forum, Phoenix, AZ, May*, 2006.
- [3] Hirschberg, M., "On Wind Tunnel Tests and Computations Concerning the Problem of Shrouded Propellers," *Vertiflite*, 2016, pp. 10–11.

- [4] Kruger, W., "On Wind Tunnel Tests and computations Concerning the Problem of Shrouded Propellers - TN 1202," Tech. rep., NACA, 1949.
- [5] Leishman, J. G., *Principles of Helicopter Aerodynamics*, 2nd ed., Cambridge University Press, 2006.
- [6] Pereira, J. and Chopra, I., "Surface Pressure Measurements on an MAV-Scale Shrouded Rotor in Hover," *American Helicopter Society 62nd Annual Forum, Phoenix, AZ*, 2006.
- [7] Pereira, J. and Chopra, I., "Performance and Surface Pressure Measurements on a MAV-Scale Shrouded Rotor in Translational Flight," *American Helicopter Society 63rd Annual Forum, Virginia Beach, VA*, 2007.
- [8] Hook, R., Myers, L., and McLaughlin, D., "Investigation on Flow Physics of Edgewise Ducted rotor Air Vehicles," *American Helicopter Society 67th Annual Forum, Virginia Beach, VA*, 2011.
- [9] Hook, R., Myers, L., and McLaughlin, D., "A Study of Leading Edge Shapes for the Front Duct of a Dual Ducted Rotor Vehicle," *American Helicopter Society 67th Annual Forum, Virginia Beach, VA*, 2011.
- [10] Martin, P., and Tung, C., "Performance and Flowfield Measurements on a 10-inch Ducted Rotor VTOL UAV," *American Helicopter Society 60th Annual Forum, Baltimore, MD, June*, 2004.
- [11] Martin, P., and Boxwell, D., A., "Design, Analysis and Experiments on a 10-Inch Ducted Rotor VTOL UAV," *American Helicopter Society International Specialists Meeting on Unmanned Rotorcraft: Design, Control and Testing, Chandler, AZ, Jan*, 2005.
- [12] Akturk, A., and Camci, C., "Influence of Tip Clearance and Inlet Flow Distortion on Ducted rotor Performance in VTOL UAVs," *American Helicopter Society 66th Annual Forum, Phoenix, AZ*, 2010.
- [13] Akturk, A., and Camci, C., "Experimental and Computational Assessment of a Ducted-Fan Rotor Flow Model," *Journal of Aircraft*, Vol. 49, No. 3, 2012, pp. 885–897.
- [14] Akturk, A., and Camci, C., "Lip separation and Inlet Flow Distortion Control in Ducted Fans Used in VTOL Systems," *ASME Turbo Expo, Dusseldorf, Germany*, 2014.
- [15] Singh, R., and Dinavahi, S., "Shape Optimization of a Ducted Rotor System for Aerodynamic Performance," *49th AIAA Aerospace Sciences Meeting, Orlando, FL*, 2011.
- [16] Jimenez, B., and Singh, R., "Effect of Duct-Rotor Aerodynamic Interactions on Blade Design for Hover and Axial Flight," *53rd AIAA Aerospace Sciences Meeting, AIAA SciTech, Kissimmee, FL*, 2015.
- [17] Misiorowski, M., Gandhi, F., and Oberai, A., "Computational Analysis and Flow Visualization of Ducted Rotors in Edgewise Flight," *American Helicopter Society 73rd Annual Forum, Fort Worth, TX*, 2017.
- [18] Advanced Precision Composites - Propellers, "Performance Data - 12x5.5 MR," Tech. rep., APC, 2014. URL apcserve.w20.wh-2.com/v/PERFILES_WEB/PER3_12x55MR.dat.
- [19] Corson, D., Rajeev, J., and Farzin, S., "Industrial Application of RANS Modeling: Capabilities and Needs," *International Journal of Computational Fluid Dynamics*, Vol. 23, No. 4, 2009, pp. 337–347.
- [20] Simmetrix, "MeshSim – Automatic Mesh Generation," May 1997. URL <http://www.simmetrix.com/products/SimulationModelingSuite/MeshSim/MeshSim.html>.
- [21] Jansen, K., E., Whiting, C., H., and Hulbert, G., M., "A Generalized- α Method for Integrating the Filtered Navier-Stokes Equations with a Stabilized Finite Element Method," *Computer Methods in Applied Mechanics and Engineering*, Vol. 190, No. 3, 2000, pp. 305–319.
- [22] Brooks, A., N., and Hughes, T., J., "Streamline Upwind/Petrov-Galerkin Formulations for Convection Dominated Flows with Particular Emphasis on the Incompressible Navier-Stokes Equations," *Computer Methods in Applied Mechanics and Engineering*, Vol. 32, No. 1-3, 1982, pp. 199–259.